JOURNAL OF GEOPHYSICAL RESEARCH, VOL. 115, B00B02, doi:10.1029/2009JB006969, 2010

Ground surface deformation patterns, magma supply, and magma storage at Okmok volcano, Alaska, from InSAR analysis: 1. Intereruption deformation, 1997–2008

Zhong Lu,[1,2] Daniel Dzurisin,[1] Juliet Biggs,[3] Charles Wicks Jr.,[4] and Steve McNutt[5]

Received 9 September 2009; revised 20 November 2009; accepted 18 December 2009; published 5 May 2010.

[1] Starting soon after the 1997 eruption at Okmok volcano and continuing until the start of the 2008 eruption, magma accumulated in a storage zone centered ~3.5 km beneath the caldera floor at a rate that varied with time. A Mogi-type point pressure source or finite sphere with a radius of 1 km provides an adequate fit to the deformation field portrayed in time-sequential interferometric synthetic aperture radar images. From the end of the 1997 eruption through summer 2004, magma storage increased by 3.2–4.5 × 10^7 m^3, which corresponds to 75–85% of the magma volume erupted in 1997. Thereafter, the average magma supply rate decreased such that by 10 July 2008, 2 days before the start of the 2008 eruption, magma storage had increased by 3.7–5.2 × 10^7 m^3 or 85–100% of the 1997 eruption volume. We propose that the supply rate decreased in response to the diminishing pressure gradient between the shallow storage zone and a deeper magma source region. Eventually the effects of continuing magma supply and vesiculation of stored magma caused a critical pressure threshold to be exceeded, triggering the 2008 eruption. A similar pattern of initially rapid inflation followed by oscillatory but generally slowing inflation was observed prior to the 1997 eruption. In both cases, withdrawal of magma during the eruptions depressurized the shallow storage zone, causing significant volcano-wide subsidence and initiating a new intereruption deformation cycle.

Citation: Lu, Z., D. Dzurisin, J. Biggs, C. Wicks Jr., and S. McNutt (2010), Ground surface deformation patterns, magma supply, and magma storage at Okmok volcano, Alaska, from InSAR analysis: 1. Intereruption deformation, 1997–2008, *J. Geophys. Res.*, *115*, B00B02, doi:10.1029/2009JB006969.

1. Introduction and Previous Work

[2] Okmok is a dominantly basaltic central volcanic complex that occupies most of the northeastern end of Umnak Island, Alaska, in the central Aleutian volcanic arc. Catastrophic pyroclastic eruptions circa 12.0 and 2.05 ka resulted in the formation of two overlapping summit calderas [*Miller et al.*, 1998]. The caldera complex was breached along its north rim by one or more catastrophic floods between 1.4 and 1.0 ka [*Larsen et al.*, 2009]. Subsequent eruptions produced a field of small cones and lava flows, including several historically active vents within the younger caldera. Cone A on the southwestern edge of the caldera floor (Figure 1) is the youngest cone on the volcano and formed almost entirely during the 20th century [*Grey*, 2003]. Cone D on the east-central caldera floor (Figure 1) is about 1000 years old and its deposits suggest highly explosive interactions between magma, groundwater, and surface water [*Larsen et al.*, 2009]. In addition to many minor explosive eruptions at Cone A, blocky basaltic lava flows were extruded there during large effusive eruptions in 1945, 1958, and 1997 (Figure 1).

[3] The 1997 eruption of Okmok was a moderate Hawaiian to Strombolian type with an ash plume that reached 10 km altitude. The eruption began in early February 1997 and ended in late April 1997 [*Miller et al.*, 1998; *Patrick et al.*, 2003]. The 1997 lava flows traveled about 6 km, partly overriding the 1958 flows, and are generally similar to the a′a′ flows from the 1945 and 1958 eruptions. By differencing pre- and posteruption digital elevation models (DEMs) that were generated from interferometric synthetic aperture radar (InSAR) imagery, *Lu et al.* [2003b] mapped the three-dimensional distribution of the 1997 lava flow. The estimated average and maximum thicknesses of the 1997 flows are 17 and 50 m, respectively. The 1997 flows cover about 8.9 km^2, with an estimated bulk volume of 0.154 ± 0.025 km^3 [*Lu et al.*, 2003b].

[4] A hydrovolcanic eruption from near Cone D began on 12 July 2008, and continued until late August 2008. This paper addresses Okmok deformation measured with InSAR observations from the end of the 1997 eruption to 10 July

[1]Cascades Volcano Observatory, U.S. Geological Survey, Vancouver, Washington, USA.
[2]EROS Center, U.S. Geological Survey, Vancouver, Washington, USA.
[3]Rosenstiel School of Marine and Atmospheric Sciences, University of Miami, Miami, Florida, USA.
[4]U.S. Geological Survey, Menlo Park, California, USA.
[5]Alaska Volcano Observatory, University of Alaska Fairbanks, Fairbanks, Alaska, USA.

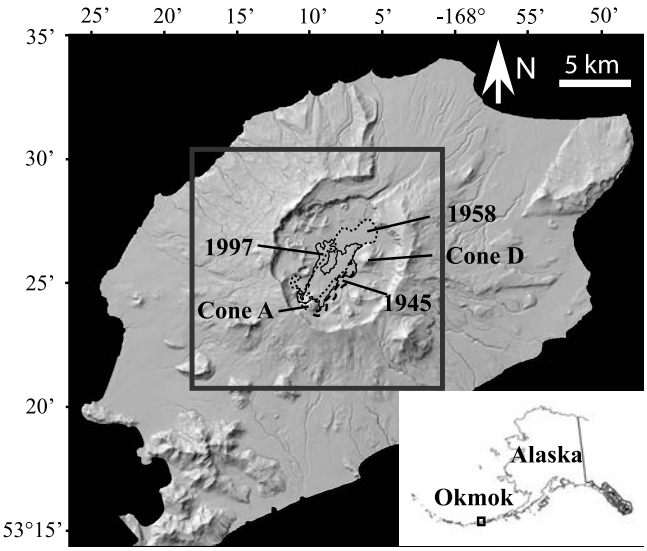

Figure 1. Shaded relief image of Okmok volcano. Cone A and Cone D are vents for historical eruptions. Inset shows location of Okmok in the central Aleutian volcanic arc. The rectangle represents the coverage of InSAR images shown in Figures 2–5. Also shown are outlines of lava flows emplaced in 1945, 1958, and 1997.

2008, shortly before the onset of the 12 July 2008 eruption. Results of our study of deformation that occurred during the 2008 eruption are reported in a separate paper [*Lu and Dzurisin*, 2010].

[5] Deformation of Okmok volcano has been studied using both InSAR images acquired before the fall of 2003 [*Lu et al.*, 1998, 2000, 2005; *Mann et al.*, 2002] and GPS measurements made during 2000–2007 [*Miyagi et al.*, 2004; *Fournier et al.*, 2009]. The uplift rate within the caldera before the February–April 1997 eruption ranged from more than 14 cm/y during 1992–1993 to about 3 cm/y during 1993–1995. The caldera floor subsided 1–2 cm during the time interval from 1.5 to 0.5 years before the start of the 1997 eruption, and more than 1.2 m during the eruption itself [*Lu et al.*, 2005]. Okmok began to reinflate soon after the 1997 eruption. Based on the shape and radial pattern of the displacement field from InSAR observations before 2003, *Lu et al.* [2005] modeled the source as a point source or spherical magma reservoir [*Mogi*, 1958] located beneath the center of the caldera at a depth of 2.6–3.2 km below sea level (3.1–3.7 km beneath the caldera floor). The three-dimensional position of the source for pre-eruptive inflation, coeruptive deflation, and posteruptive inflation did not change significantly during the 11 year period of the InSAR study (1992–2003). Analysis of GPS data acquired during 2000–2007 led to a similar conclusion [*Miyagi et al.*, 2004; *Fournier et al.*, 2009], and our results presented in this paper show that the same holds true for 2003–2008.

[6] For this paper, we analyzed all available synthetic aperture radar (SAR) images of Okmok acquired during 1997–2008 by three different satellite sensors to investigate intereruption deformation patterns. In addition to reanalyzing some of the 1997–2003 images studied by *Lu et al.* [2005], we analyzed more than 90 InSAR images for the period 2003–2008. Included in the InSAR data set are several images for the time period from summer 2007 to 10 July 2008, just 2 days before the start of the 2008 eruption, for which neither InSAR nor GPS results have been reported previously. Using averaged interferograms from 9 tracks with different InSAR viewing geometries, we compared best fit source parameters using a Mogi point source [*Mogi*, 1958] and a vertical prolate uniformly pressured spheroid source [*Yang et al.*, 1988]. We found that the spheroid source, with more degrees of freedom, did not significantly improve the model's goodness of fit, and therefore we chose to use the simpler Mogi source for subsequent analysis. We investigated the stability of the deformation source using 150 InSAR images and found that the location of the source did not change significantly during the period of study. Using magma-intrusion volume estimates from multiple interferograms that overlap in time, we conducted a time series analysis that accounts for realistic uncertainties associated with the volume estimates. Based on those results, we discuss the possible configuration and dynamics of Okmok's magma plumbing system as inferred from surface deformation patterns during an entire intereruption deformation cycle.

2. InSAR Data and Analysis

[7] SAR images used for this study were acquired by European Space Agency (ESA) Envisat and ERS-2, and by Canadian Space Agency (CSA) Radarsat-1, during both descending and ascending passes. The sensors aboard all three satellites are C band SARs operating at a wavelength of 56.6 mm (ERS-2 and Radarsat-1) or 56.3 mm (Envisat). The Envisat images are standard beam 2 with radar look angles in the range 21.2°–25.0°, which is similar to ERS-2 standard beam mode (Table 1). Radarsat-1 images are from standard beam 6 with radar look angles of about 44°. The Envisat images are from 2 descending tracks and 3 ascending tracks. ERS-2 images are from 3 descending tracks and 2 ascending tracks. Radarsat-1 images are from 1 descending and 1 ascending track. Taken as a whole, these images constitute 9 different imaging geometries. Because snow and ice on Aleutian volcanoes cause interferometric coherence to be lost except during summer, we used images acquired only between early June and early November of each year from 1997 to 2008.

[8] The data set analyzed here includes 150 InSAR images with time separations from about 1 to about 4 years. Atmospheric delay anomalies can be strong in radar interferograms for the Aleutian region [*Lu et al.*, 2003a, 2005], to the extent that often they are the dominant signal in interferograms that span only a few months. Therefore, we did not include in our study interferograms that span less than about 9 months, except for a few that span June–July 2008 just prior to the eruption that began on 12 July 2008.

[9] Sequential 1 year interferograms for Okmok volcano from 1997 to 2008 show that the surface inflation rate generally decreased with time during 1997–2001 (Figures 2a–2d): from ~10 cm/y during 1997–1998, to ~8 cm/y during 1998–2000, and ~4 cm/y during 2000–2001. Then the inflation rate increased to ~12 cm/y during 2001–2002 (Figure 2e) and reached a maximum of ~17–20 cm/y during 2002–2004 (Figures 2f and 2g). The inflation trend was interrupted during 2004–2005, when ~3–5 cm of subsidence occurred (Figure 2h). A similar amount of uplift occurred

Table 1. SAR Images Used for This Study[a]

Master Date	Slave Date	Satellite/Track ID	Track Angle (°)	Look Angle (°)	B_n (m)
19970701	19980825	E115	−166.8	21.5	236
19970701	19990706	E115	−166.8	21.5	−119
19970717	19980910	E344	−166.8	24	69
19970717	20000914	E344	−166.8	24	−41
19970909	19980929	E115	−166.8	21.5	190
19970909	20000829	E115	−166.8	21.5	−80
19970925	19980910	E344	−166.8	24	92
19970925	19990617	E344	−166.8	24	−25
19970925	20000914	E344	−166.8	24	−18
19980825	20001003	E115	−166.8	21.5	−11
19980910	19990930	E344	−166.8	24	295
19980910	20000914	E344	−166.8	24	−110
19980929	19990601	E115	−166.8	21.5	77
19980929	20000829	E115	−166.8	21.5	−270
19980929	20001107	E115	−166.8	21.5	−147
19980929	20010710	E115	−166.8	21.5	120
19981031	20010915	E072	−166.8	25	−11
19981103	20010710	E115	−166.8	21.5	−90
19990617	20000706	E344	−166.8	24	−217
19990617	20000914	E344	−166.8	24	7
19990706	20000725	E115	−166.8	21.5	47
19990807	20010915	E072	−166.8	25	−283
19990903	20000818	E451	−13.3	23	108
19990914	20000725	E115	−166.8	21.5	274
19990930	20020815	E344	−166.8	24	−79
19990930	20020919	E344	−166.8	24	33
20000725	20030715	E115	−166.8	21.5	149
20000731	20010702	RSAT	−8.9	44.1	65
20000818	20020719	E451	−13.3	23	8
20000824	20010702	RSAT	−8.9	44.1	−10
20000824	20010702	RSAT	−171.2	44	−9
20000826	20010915	E072	−166.8	25	394
20000906	20040811	E222	−13.3	25	−112
20000917	20010819	RSAT	−171.2	44	362
20000917	20010912	RSAT	−171.2	44	350
20000927	20010829	RSAT	−8.9	44.1	336
20001107	20010710	E115	−166.8	21.5	−267
20001107	20021008	E115	−166.8	21.5	203
20010702	20020814	RSAT	−8.9	44.1	161
20010710	20020625	E115	−166.8	21.5	−211
20010710	20021008	E115	−166.8	21.5	−80
20010710	20041012	E115	−166.8	21.5	27
20010726	20020627	RSAT	−8.9	44.1	207
20010915	20021109	E072	−166.8	25	93
20020625	20041012	E115	−166.8	21.5	238
20020711	20040715	E344	−166.8	24	247
20020719	20040827	E451	−13.3	23	−159
20020730	20040629	E115	−166.8	21.5	134
20020814	20030902	RSAT	−8.9	44.1	−152
20020815	20031009	E344	−166.8	24	−86
20020907	20030902	RSAT	−8.9	44.1	119
20020907	20030926	RSAT	−8.9	44.1	71
20020927	20041001	E451	−13.3	23	104
20021001	20030926	RSAT	−8.9	44.1	197
20021008	20030923	E115	−166.8	21.5	143
20030702	20040720	RSAT	−171.2	44	115
20030702	20041024	RSAT	−171.2	44	−104
20030704	20040723	E451	−13.3	23	−36
20030715	20040629	V115	−168.8	21.5	−31
20030716	20040710	RSAT	−8.9	44.1	−282
20030716	20040803	RSAT	−8.9	44.1	−20
20030716	20040827	RSAT	−8.9	44.1	−69
20030726	20040720	RSAT	−171.2	44	−96
20030731	20040819	V344	−166.8	24	193
20030731	20050908	V344	−166.8	24	152
20030731	20051013	V344	−166.8	24	195
20030809	20040710	RSAT	−8.9	44.1	−170
20030809	20040803	RSAT	−8.9	44.1	92
20030809	20040827	RSAT	−8.9	44.1	43
20030809	20041014	RSAT	−8.9	44.1	−365
20030819	20040720	RSAT	−171.2	44	119
20030819	20040907	E115	−166.8	21.5	−74

Table 1. (continued)

Master Date	Slave Date	Satellite/Track ID	Track Angle (°)	Look Angle (°)	B_n (m)
20030819	20050927	E115	−166.8	21.5	−5
20030819	20050927	V115	−168.8	21.5	91
20030902	20040710	RSAT	−8.9	44.1	303
20030902	20040920	RSAT	−8.9	44.1	−117
20030902	20041014	RSAT	−8.9	44.1	108
20030904	20040715	E344	−166.8	24	44
20030904	20050630	E344	−166.8	24	206
20030912	20040906	RSAT	−171.2	44	184
20030912	20040930	RSAT	−171.2	44	−37
20030912	20040723	E451	−13.3	23	248
20030920	20041009	E072	−166.8	25	17
20030923	20041012	V115	−168.8	21.5	−38
20030926	20040710	RSAT	−8.9	44.1	351
20030926	20040920	RSAT	−8.9	44.1	−69
20030926	20041014	RSAT	−8.9	44.1	156
20031001	20040811	E222	−13.3	25	−276
20031006	20040906	RSAT	−171.2	44	49
20031009	20060824	E344	−166.8	24	59
20031009	20060824	V344	−166.8	24	168
20031028	20040629	V115	−168.8	21.5	129
20031030	20040906	RSAT	−171.2	44	−224
20031030	20041024	RSAT	−171.2	44	108
20040602	20050621	RSAT	−171.2	44	−182
20040626	20050715	RSAT	−171.2	44	128
20040710	20050822	RSAT	−8.9	44.1	223
20040710	20060630	RSAT	−8.9	44.1	8
20040720	20050715	RSAT	−171.2	44	−98
20040803	20050705	RSAT	−8.9	44.1	227
20040803	20050719	E115	−166.8	21.5	264
20040819	20051013	V344	−166.8	24	1
20040827	20050822	RSAT	−8.9	44.1	10
20040827	20060901	V451	−13.3	23	−76
20040907	20050927	E115	−166.8	21.5	69
20040907	20050719	V115	−168.8	21.5	−284
20040907	20060808	V115	−168.8	21.5	−112
20040915	20050831	E222	−13.3	25	9
20040920	20050915	RSAT	−8.9	44.1	−60
20040930	20050925	RSAT	−171.2	44	−285
20041001	20060728	V451	−13.3	23	59
20041012	20050614	V115	−168.8	21.5	34
20041014	20050915	RSAT	−8.9	44.1	−285
20041014	20051102	RSAT	−8.9	44.1	150
20041020	20060712	V222	−13.3	25	155
20041024	20050715	RSAT	−171.2	44	119
20041024	20060827	RSAT	−171.2	44	−125
20050622	20071010	V222	−13.3	25	44
20050630	20060824	V344	−166.8	24	64
20050630	20070913	V344	−166.8	24	−90
20050715	20060803	RSAT	−171.2	44	37
20050715	20060827	RSAT	−171.2	44	−244
20050719	20060704	V115	−168.8	21.5	36
20050719	20060808	V115	−168.8	21.5	171
20050719	20060912	V115	−168.8	21.5	−175
20050812	20070817	E451	−13.3	23	99
20050812	20070921	V451	−13.3	23	−223
20050822	20060817	RSAT	−8.9	44.1	−170
20050915	20060724	RSAT	−8.9	44.1	149
20050927	20071002	V115	−168.8	21.5	54
20051013	20060615	V344	−166.8	24	177
20060615	20070705	V344	−166.8	24	−2
20060623	20070817	E451	−13.3	23	65
20060710	20070822	RSAT	−171.2	44	−86
20060720	20070913	V344	−166.8	24	−212
20060803	20070915	RSAT	−171.2	44	81
20060816	20070801	V222	−13.3	25	373
20060816	20071010	V222	−13.3	25	18
20060817	20070719	RSAT	−8.9	44.1	−58
20060901	20070817	E451	−13.3	23	−220
20060901	20070921	V451	−13.3	23	329
20060910	20070929	RSAT	−8.9	44.1	141
20060920	20070822	RSAT	−171.2	44	−283
20061017	20070828	E115	−166.8	21.5	−19

Table 1. (continued)

Master Date	Slave Date	Satellite/Track ID	Track Angle (°)	Look Angle (°)	B_n (m)
20061022	20071007	V179	−13.2	21.2	−32
20070705	20080619	V344	−166.8	24	123
20070713	20080627	E451	−13.3	23	−190
20071002	20080708	V115	−168.8	21.5	368
20071026	20080627	V451	−13.3	23	−5
20080603	20080708	V115	−168.8	21.5	127
20080616	20080710	RSAT	−11.3	33.8	−276

[a]Dates are image acquisition times in yyyymmdd format (read 19970701 as 1 July 1997). Also included are satellite ID (E is ERS-2, V is Envisat, and RSAT is Radarsat-1), track ID (072, 115, 179, 344, and 451), satellite track angle, and SAR look angle at which the images were acquired. B_n is the perpendicular baseline of the corresponding InSAR pair.

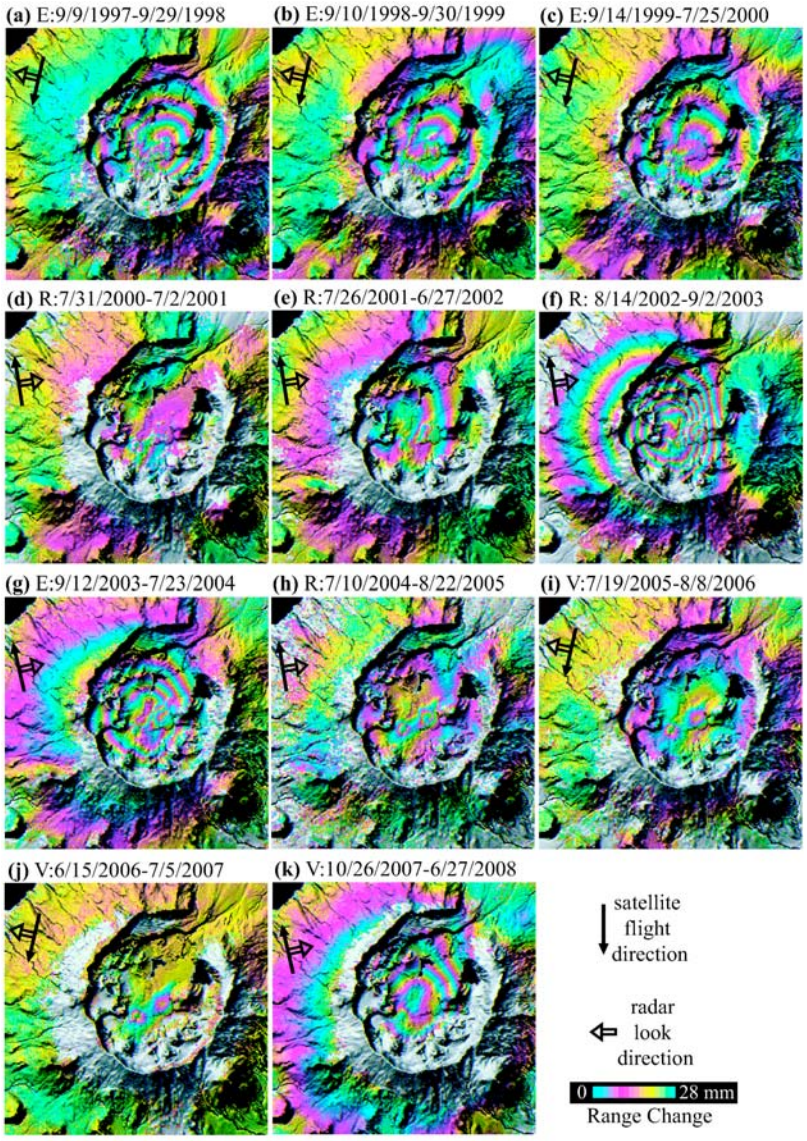

Figure 2. Annual interferograms showing ground surface deformation of Okmok volcano from 1997 to 2008, specifically during the following time periods (date format here is yyyymmdd): (a) 19970909–19980929, (b) 19980910–19990930, (c) 19990914–20000725, (d) 20000731–20010702, (e) 20010726–20020627, (f) 20020814–20030902, (g) 20030912–20040723, (h) 20040710–20050822, (i) 20050719–20060808, (j) 20060615–20070705, and (k) 20071026–20080627. Satellite ID (E is ERS-2, R is Radarsat-1, and V is Envisat), satellite flight direction, and radar look direction are labeled. Each fringe (full color cycle) represents 28 mm of range change between the ground and the satellite. Additional information on SAR images used to produce the interferograms is given in Table 1. Areas that lack interferometric coherence are uncolored.

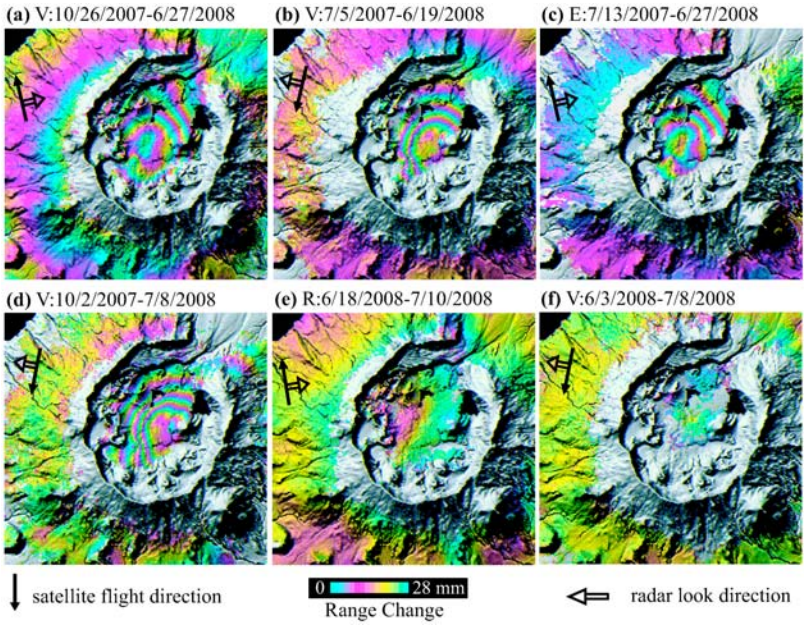

Figure 3. Interferograms spanning the following periods during the year preceding the 12 July 2008 eruption at Okmok (date format here is yyyymmdd): (a) 20071026–20080627 (Envisat Track 451), (b) 20070705–20080619 (Envisat Track 344), (c) 20070713–20080627 (ERS–2 Track 451), (d) 20071002–20080708 (Envisat Track 115), (e) 20080616–20080710 (Radarsat-1 Ascending Track), and (f) 20080603–20080708 (Envisat Track 115). Satellite ID (E is ERS-2, R isRadarsat-1, and V is Envisat), satellite flight direction and radar look direction are labeled. Each fringe (full color cycle) represents 28 mm of range change between the ground and the satellite. Areas that lack interferometric coherence are uncolored.

during 2005–2006 (Figure 2i), followed by nearly no volcano-wide deformation during 2006–2007 (Figure 2j). About 15 cm of uplift occurred from summer 2007 to 10 July 2008, shortly before the 12 July 2008 eruption (Figure 2k).

[10] Interferograms from different sensors/tracks (Figure 3) confirm that the inflation rate at Okmok during 2007–2008 was the greatest since 2002–2004. We were fortunate to obtain two images acquired on 8 and 10 July 2008 (Figures 3e and 3f), just a few days prior to the 12 July 2008 eruption. InSAR images that span 30–40 days immediately before the eruption (Figures 3e and 3f) indicate an inflation rate that is similar to that for interferograms that span a full year prior to the eruption (Figures 3a–3d). This suggests that the inflation rate did not change markedly during the month before the 2008 eruption began, which is consistent with independent continuous GPS observations [*Freymueller et al.*, 2008; *Larsen et al.*, 2009].

3. Deformation Modeling, Error Estimation, and Analysis

3.1. Source Geometry

[11] Previously, deformation data sets for Okmok volcano have been modeled using a point source within a homogenous isotropic elastic half-space [*Mogi*, 1958], which fits well the campaign GPS data for 2000–2002 [*Miyagi et al.*, 2004], continuous GPS (CGPS) data for 2002–2007 [*Fournier et al.*, 2009], and InSAR data for 1992–2003 [*Lu et al.*, 1998, 2000, 2005; *Mann et al.*, 2002; *Masterlark*, 2007]. To explore whether a more complicated source geometry would provide a better fit to the complete InSAR data set, we created an average interferogram for each of the 9 tracks included in our study (Figure 4a). This approach was made possible by the high quality of the interferograms, in which more than 75% of pixels corresponding to Okmok Island are coherent. We modeled the averaged interferograms using both a tension sphere source [*Mogi*, 1958] and a vertical uniformly pressured prolate spheroid source [*Yang et al.*, 1988; *Fialko and Simons*, 2000]. For each interferogram, we determined best fit parameters for the location (horizontal coordinates and depth) and "strength" (volume or pressure change) of the deformation source by assuming the magma residing in the reservoir is incompressible. For a discussion on how magma compressibility affects deformation modeling results, please refer to the papers by *Johnson et al.* [2000] and *Rivalta and Segall* [2008]. To account for the effect of topography on the observed deformation field, we used the simple approach proposed by *Williams and Wadge* [1998]. We used the downhill simplex method and Monte Carlo simulations [*Press et al.*, 1992] to estimate optimal parameters, and the root-mean-square error (RMSE) between observed and modeled interferograms as the prediction fit criterion.

[12] Treating atmospheric delay artifacts as uncorrelated noise in InSAR data can result in substantial underestimates of the uncertainties in model parameters [e.g., *Jonsson*, 2002; *Wright et al.*, 2003; *Lohman and Simons*, 2005]. In this study, we estimated uncertainties for each interferogram using a Monte Carlo approach [e.g., *Wright et al.*, 2003]. We calculated representative atmospheric noise parameters for each interferogram based on the assumption that the atmospheric

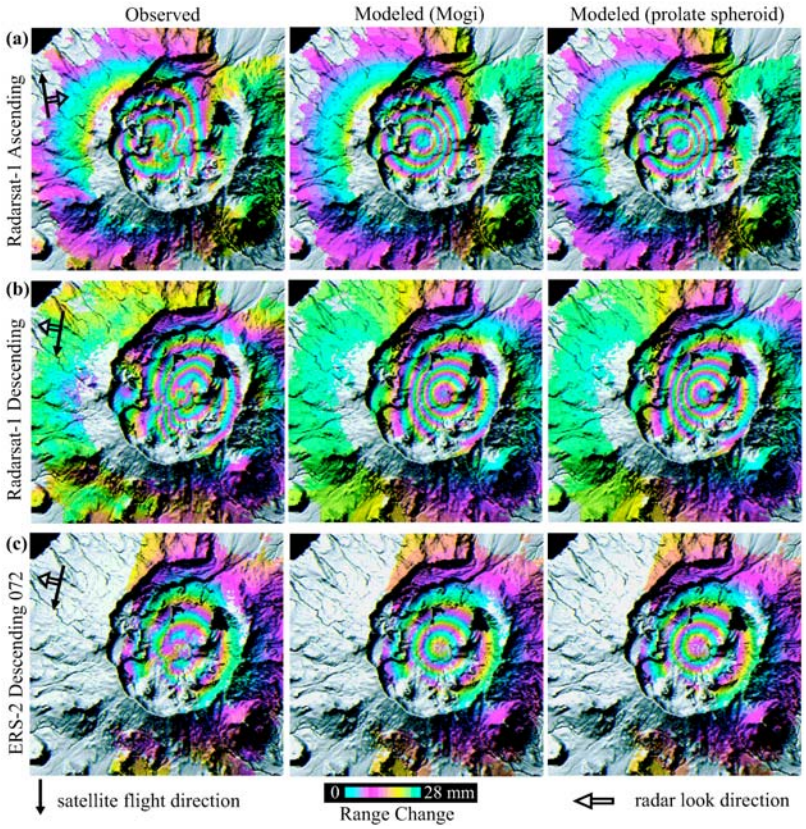

Figure 4. (left) Observed average interferograms, (middle) synthetic interferograms from a point pressure source model, and (right) synthetic interferograms from a prolate spheroid source model for the following nine satellite tracks (Table 1): (a) Radarsat-1 ascending track, (b) Radarsat-1 descending track, (c) ERS-2 descending track 072, (d) ERS-2 descending track 115, (e) ERS-2 ascending track 222, (f) ERS-2 descending track 344, (g) ERS-2 ascending track 451, (h) Envisat descending track 115, and (i) Envisat descending track 344. Satellite flight direction and radar look direction are labeled. Each fringe (full color cycle) represents 28 mm of range change between the ground and the satellite. Areas that lack interferometric coherence are uncolored.

noise structure function is homogeneous and radially symmetric across Okmok volcano. We calculated a 1-D covariance function, parameterized using an exponential Bessel function [*Biggs et al.*, 2009], using only far-field areas of each interferogram where topography-related atmospheric artifacts were modeled as a linear function of elevation and removed. Then we used the results to create 20 sets of synthetic noise for each interferogram using the method of *Wright et al.* [2003]. Finally, we calculated best fitting parameters for a Mogi-type source and a prolate spheroid source by (1) modeling each interferogram independently and (2) modeling all of the interferograms jointly (Table 2). The range of these solutions represents the sensitivity of model parameters to realistic variations in atmospheric conditions, and thus provides a better estimate of the associated uncertainties.

[13] When the averaged interferograms are modeled jointly, the best fit RMSEs for the two source types are identical at 3.5 mm (Table 2). Accordingly, the synthetic interferograms for the best fit Mogi source are indistinguishable from those for the best fit prolate spheroid source (Figures 4b and 4c). The experimental *F* test requires that, in order to be considered a significant improvement over a simpler model, any model with more degrees of freedom must provide a definable improvement in RMSE [e.g., *Gordon et al.*, 1987; *Dzurisin et al.*, 2009]. In this case, the vertical prolate spheroid model has two more degrees of freedom than the Mogi model (major and minor axes in addition to X, Y, Z coordinates), but provides no improvement in RMSE. Therefore, the spheroid model fails the experimental *F* test for significance. Note also from Table 2 that (1) the center coordinates for the two source types are nearly identical, (2) the model-derived uncertainties in the Mogi source position are about half as large as for the prolate spheroid source, and (3) the asperity ratio between the major and minor axes for the best fit prolate spheroid model is about 1.04, which corresponds very nearly to a sphere. We conclude that the magma storage zone beneath Okmok can be approximated by a sphere with a radius of about 1 km (Table 2). Therefore, and for computational simplicity, we used the *Mogi* [1958] source for all subsequent analysis of the Okmok intereruption interferograms.

3.2. Mogi Modeling of Individual Interferograms

[14] As is the case for campaign GPS and CGPS data [*Miyagi et al.*, 2004; *Fournier et al.*, 2009], the Mogi source fits the observed InSAR images well. Figure 5 shows observed

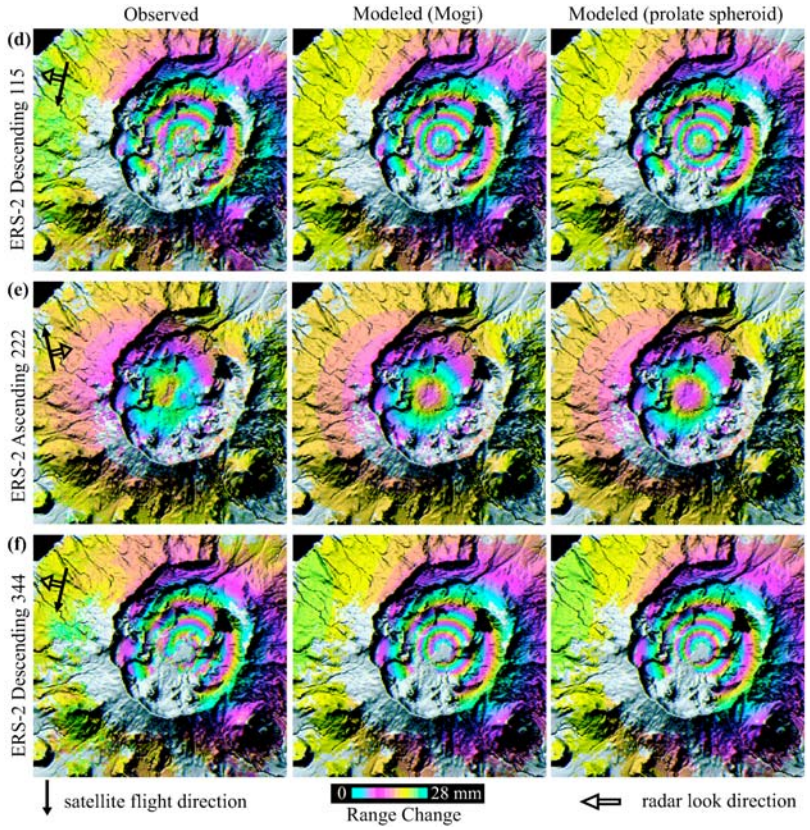

Figure 4. (continued)

(Figure 5a and 5d), modeled (Figure 5b and 5e), and residual (Figure 5c and 5f) interferograms for 1 year periods of inflation (2003–2004) and deflation (2004–2005). After volcano-wide deformation due to the best fit Mogi source is removed, residual fringes that correspond to the 1997 lava flow remain in both of the interferograms. The surface of the flow continued to subside at rates as high as 3 cm/y during 2003–2007. In fact, 2006–2007 interferograms are dominated by subsidence of the 1997 lava flow (e.g., Figure 2g).

[15] To explain persistent subsidence of the 1997 lava flow, *Lu et al.* [2005] considered the following three possible mechanisms: (1) poroelastic deformation of the caldera floor caused by the lava flow gravity load [*Wang*, 2000]; (2) thermoelastic deformation of the flow due to cooling after emplacement [*Biot*, 1956]; and (3) viscoelastic relaxation of the caldera floor caused by the lava flow gravity load [*Jaeger*, 1969; *Briole et al.*, 1997; *Stevens et al.*, 2001]. *Lu et al.* [2005] constructed two-dimensional finite element models of the deformation field for each mechanism, and concluded that the subsidence most likely was caused by a combination of thermoelastic cooling of the 1997 flow and viscoelastic relaxation of the caldera floor in response to the gravity load from both the 1997 and nearby pre-1997 flows. The same two mechanisms are the most likely explanation for subsidence observed in residual interferograms for the entire time period 1997–2008.

[16] Localized deformation of young lava flows combined with broader deformation caused by magma accumulation and withdrawal produce the complex deformation fields revealed by the 1997–2008 interferograms. The effect of lava flow contraction can last many years [e.g., *Lu et al.*, 2005]. For example, a significant amount of subsidence (1 to 2 cm/y) has been observed about 50 years after the emplacement of the 1958 lava flows at Okmok volcano [*Lu et al.*, 2005]. This has implications for positioning geodetic markers and deformation sensors at Okmok and other similar volcanoes, and for interpretation of resulting point measurement data (e.g., GPS, tilt, borehole strain). InSAR images can provide an important spatial context for such endeavors, thus helping to avoid misinterpretations caused by unrecognized deformation sources such as young flows, localized faulting, or hydrothermal activity.

[17] Our objective here was to model the source responsible for volcano-wide deformation at Okmok, so we masked the 1997 lava flow from InSAR images before modeling them to avoid any bias from flow-related deformation. A map showing the extent of the 1997 flow can be generated from the 1997 lava thickness map produced by *Lu et al.* [2003b]. Alternatively, we determined the area covered by 1997 lava by stacking interferograms that span 2005–2007. Very little volcano-wide deformation occurred during that period, so the stacked interferograms delineate the extent of the subsiding 1997 lava flow. The result is very similar to that derived from the thickness map of *Lu et al.* [2003b].

[18] Best fit Mogi source parameters for individual interferograms were analyzed to investigate the spatial stability of

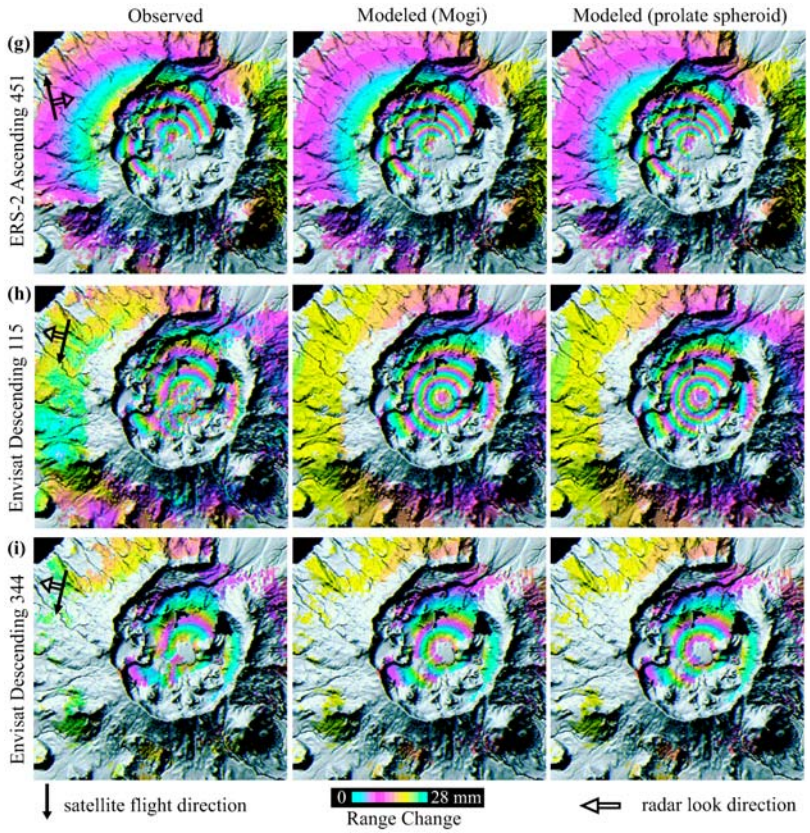

Figure 4. (continued)

the deformation source over time. Figure 6a shows the horizontal positions of the best fit sources for all of the Okmok intereruption interferograms. The sources cluster tightly near the center of the caldera. Figures 6b and 6c show time series plots of X and Y coordinates of the best fit Mogi source with respect to an arbitrary reference point (**M** in Figure 6a). Our intention in making the plots was to investigate any systematic horizontal migration of the deformation source. There is no clear trend in Y (south–north, Figure 6c), but Figure 6b shows an apparent westward migration (decreasing X) of the source by about 0.5 km from 1998 to 2008. Given the scatter in X values, the significance of this trend is open to question. However, slight westward migration of the source over time would be consistent with the observation that the 12 July 2008 deformation source is about 1 km west of the average source position from preeruption interferograms (Figure 6a [see also *Lu and Dzurisin*, 2010]). Due to large uncertainties in the modeled Mogi source position, we cannot ascertain from the interferograms whether any shift in source location occurred shortly before the 2008 eruption (Figure 6).

[19] There is no clear trend in the depth of the best fit Mogi source from 1998 to 2008; the weighted average depth is about 3 km below sea level (Figure 7a). Because the depth-strength ambiguity is inherent in inversions of a single component of three-dimensional deformation (range change, in this case) [*Dieterich and Decker*, 1975], and because a primary objective of this study was to track magma storage changes during 1997–2008 in a consistent way, we fixed the source location (X, Y, Z) to its average value from preeruption interferograms and estimated only source volume change as a function of time (Figure 7b).

3.3. Time Series Source Volume Changes

[20] We created a time series using the method of *Berardino et al.* [2002] to solve for the rate of source volume change during each time interval spanned by an interferogram using a

Table 2. Best Fit Mogi and Prolate Spheroid Source Parameters and One-Sigma Uncertainties[a]

	X (km)	Y (km)	Z (km)	Major Axis (km)	Minor Axis (km)	Best RMSE (mm^2)
			InSAR Images That are Individually Modeled			
Mogi	20.51 ± 0.13	21.80 ± 0.07	2.78 ± 0.28	NA	NA	NA
Spheroid	20.48 ± 0.26	21.85 ± 0.18	3.09 ± 0.46	2.08 ± 1.08	1.99 ± 1.02	NA
			InSAR Images That are Jointly Modeled			
Mogi	20.50 ± 0.02	21.80 ± 0.02	3.08 ± 0.05	NA	NA	3.5
Spheroid	20.48 ± 0.04	21.80 ± 0.05	3.05 ± 0.11	2.01 ± 0.34	1.94 ± 0.35	3.5

[a]RMSE is the root-mean-square error between observed and modeled interferograms. The reference for the horizontal coordinates (X, Y) is the southwestern corner of Figure 1 at geographic coordinates of N53.237794° and W168.451406°.

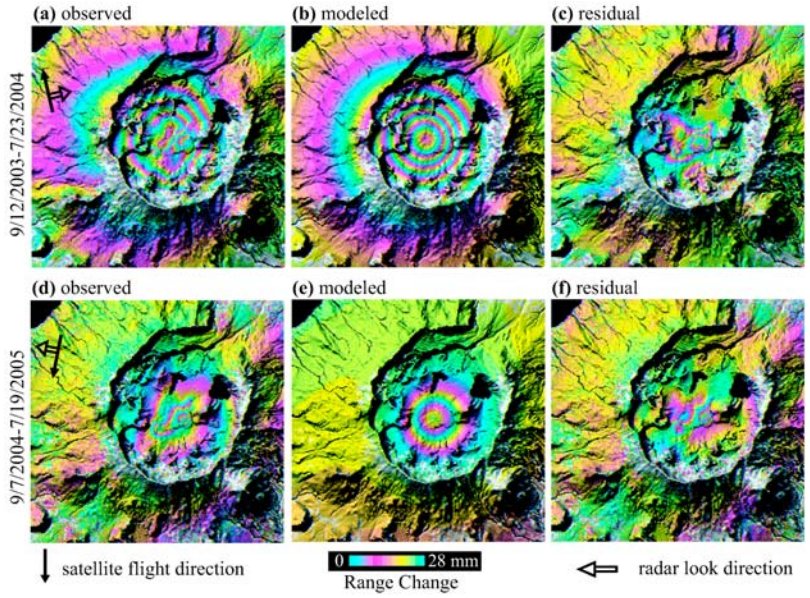

Figure 5. (a) Observed, (b) modeled, and (c) residual interferograms during a period of inflation at Okmok volcano, 12 September 2003 to 23 July 23 2004 (Table 1). (d) Observed, (e) modeled, and (f) residual interferograms during a period of deflation, 7 September 2004 to 19 July 2005 (Table 1). Satellite flight direction and radar look direction are labeled. Each fringe (full color cycle) represents 28 mm of range change between the ground and the satellite. Areas that lack interferometric coherence are uncolored.

minimum norm, singular value decomposition. This approach reduces the effect of atmospheric path delay artifacts, which usually are associated with particular epochs and are not spatially correlated through time. We weighted the solutions using the error estimate for each interferogram, as discussed above, and integrated the results to produce a time series of cumulative volume change (Figure 8). We combined error estimates for individual interferograms to estimate the uncertainty in cumulative source volume change.

[21] Magma storage beneath Okmok, as inferred from the time series plot of source volume changes (Figure 8), increased steadily from 1997 to 2001 and more rapidly during 2002–2004. Source inflation paused during 2004–2007, then resumed until the start of the 2008 eruption on 12 July. Minor amount of deflation occurred during 2004–2005, a comparable amount of inflation during 2005–2006, and nearly no deformation during 2006–2007, such that the net change in source volume during 2004–2007 was negligible. These source volume estimates from InSAR imagery match well with CGPS results for the period 2002–2007 [*Fournier et al.*, 2009]. In contrast to GPS, InSAR observations are limited in temporal resolution. Therefore, short-term fluctuations in deformation rate were possible and even likely given the GPS record [*Fournier et al.*, 2009].

4. Discussion

4.1. Capacity of the Okmok Magma Reservoir and Timing of the 2008 Eruption

[22] Our analysis indicates that the source location responsible for surface deformation at Okmok during 1997–2008 was the same one that was active during the 1997 and 2008 eruptions [*Lu et al.*, 2005; *Lu and Dzurisin*, 2010; *Mann et al.*, 2002]. This source, which we interpret as a magma storage zone, is centered ~3.5 km beneath the center of the 10 km wide caldera floor. Modeling of the deformation field indicates that the magma reservoir is approximated by a sphere with a radius of ~1 km. The source inflation/deflation rate was not steady during 1997–2008, suggesting a time-variant magma supply rate to the shallow storage zone beneath Okmok. We infer that, when the magma pressure within the reservoir reached a threshold in July 2008, an eruption ensued. Withdrawal of magma during the eruption depressurized the reservoir, causing volcano-wide subsidence and initiating a new intereruption deformation cycle.

[23] Source parameters for periods of inflation and deflation are similar, so we attribute both processes to the same source, i.e., a magma storage zone in the upper crust. Inflation occurs when magma accumulates in storage zone, presumably from a magma production zone in the lower crust or upper mantle. Deflation occurs rapidly during eruptions and at a lower rate during periods between eruptions when the magma supply rate is low enough. Using the amount of subsidence observed during 2004–2005 and constraints on magma composition from petrologic analysis of 1997 lava, *Fournier* [2008] calculated the volatile content of intruding magma to be greater than ~4.5 wt.% H_2O. During periods when the magma supply rate to the reservoir is low (e.g., 2004–2005), we envision that outgassing of H_2O, CO_2, and sulfur gases is sufficient to cause net deflation and surface subsidence. Most of the time between eruptions, the magma supply rate is high enough to overcome this effect and cause net inflation.

[24] Assuming that deformation was elastic and ignoring any differences in strength or compressibility between the magma reservoir and its host rock, the source volume change associated with the 1997 eruption was $-4.7 \pm 0.5 \times 10^7$ m^3 [*Lu et al.*, 2005]. From the end of that eruption through summer

2004, the source volume increased by 3.2–4.5 × 10^7 m^3 (i.e., 75–85% of the source volume decrease associated with the 1997 eruption). By summer 2004, the upper bound of the estimated magma volume added to the reservoir since the end of the 1997 eruption was slightly more than the lower bound of the estimated magma volume withdrawn from the reservoir during that eruption (Figure 8). By 10 July 2008, we estimate that 3.7–5.2 × 10^7 m^3 of magma had been added to the reservoir since the end of the 1997 eruption (i.e., 85–100% of the magma withdrawn during the eruption). In other words, our analysis indicates that the volume of magma withdrawn from the reservoir during the 1997 eruption was mostly replenished by July 2008 and possibly as early as summer 2004. This suggests that the timing of the 2008 eruption was determined in part by the time required to replenish the reservoir after the 1997 eruption, and hints at the existence of a threshold beyond which reservoir capacity is exceeded and an intrusion or eruption is likely to ensue.

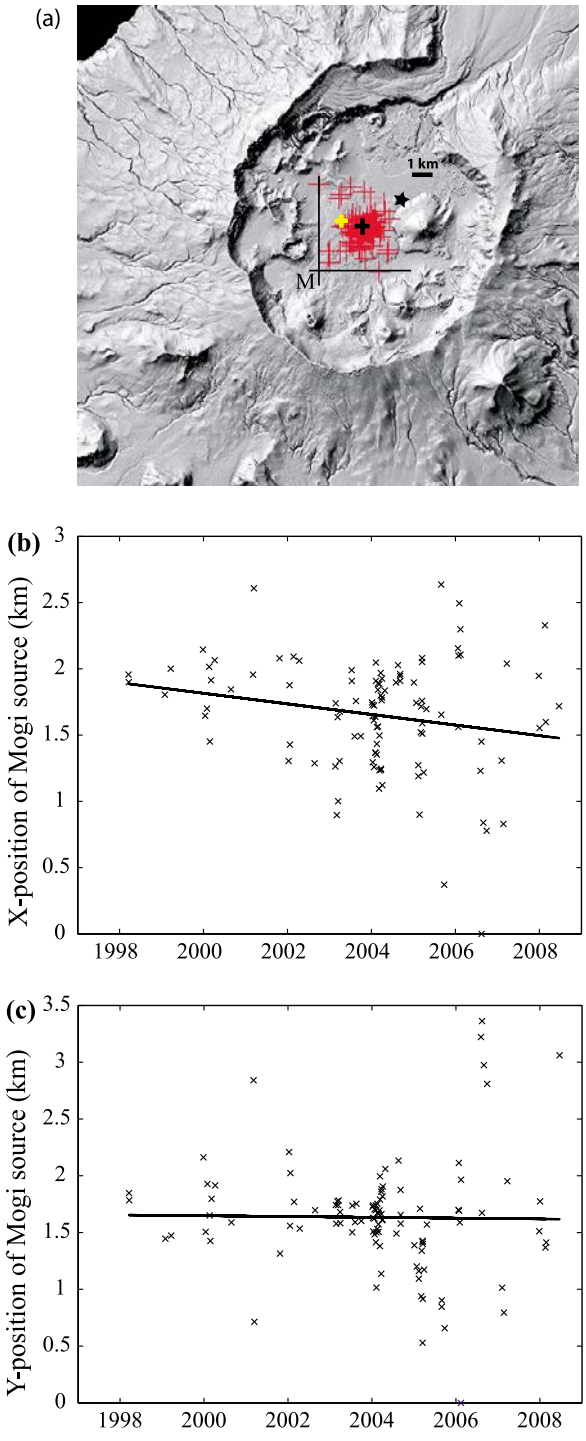

Figure 6. (a) Best fit Mogi source horizontal locations (X is easting and Y is northing) for interferograms acquired from 1997 to 2008 (Table 1), superimposed on a shaded relief image of Okmok volcano. Black cross represents the average position of the deformation sources from individual interferograms and yellow cross the average position of the deformation sources from the 2008 eruption interferograms [*Lu and Dzurisin*, 2010]. Star represents the location of 2008 vent. (b) Change in X position of the best fit Mogi source as a function of time, plotted relative to an arbitrary reference point **M** that is shown in Figure 6a. (c) Change in Y position of the best fit Mogi source as a function of time, plotted as in Figure 6b. East and north are taken as positive for the time series plots. The synthetic interferograms in Figure 4 are from the best fit solutions using the average position of the deformation sources during 1997–2008 (black cross in Figure 6a and see also Table 2).

4.2. Shallow Magma Plumbing System and Eruption Triggering Mechanism

[25] We speculate that an intracaldera ring fracture system beneath Okmok caldera provides magma migration pathways from the storage zone to vents inside the caldera. The occurrence of several eruptions in succession at Cone A during the 20th century indicates that the same pathway can endure for decades. The existence of more than one intracaldera vent (Cones A and D) and the occurrence of the 2008 eruption near Cone D indicate that the preferred magma migration path eventually changes. Which pathway is activated in a given eruption might be determined by the reservoir pressure and the relative strengths of potential pathways, i.e., portions of the ring fracture. If so, repeated eruptions from the same vent might be expected until its feeder becomes blocked during a long repose or by some other change that favors an alternative magma migration path.

[26] Taken at face value, our results indicate that the amount of magma stored at shallow depth beneath Okmok did not increase appreciably during 2004–2007, following a period of steady accumulation that began soon after the 1997 eruption ended (Figure 8). This is reminiscent of the pattern observed before the 1997 eruption. In that case, the average surface uplift rate decreased from ~10 cm/y during 1992–1993 to 2–3 cm/y during 1993–1995, and the surface subsided at an average rate of 1–2 cm/y during 1995–1996 [*Lu et al.*, 2005]. Declining inflation rates that last for a few years prior to eruptions also have been observed at other shield volcanoes [*Dvorak and Dzurisin*, 1997] including Westdahl, which is located about 200 km northeast of Okmok [*Lu et al.*, 2003a]. The diminishing pressure gradient between a shallow magma reservoir and its deeper source region while the reservoir is inflating and pressurizing could account for a decreasing magma supply rate as an eruption approaches [*Dvorak and Okamura*, 1987]. The absence of significant

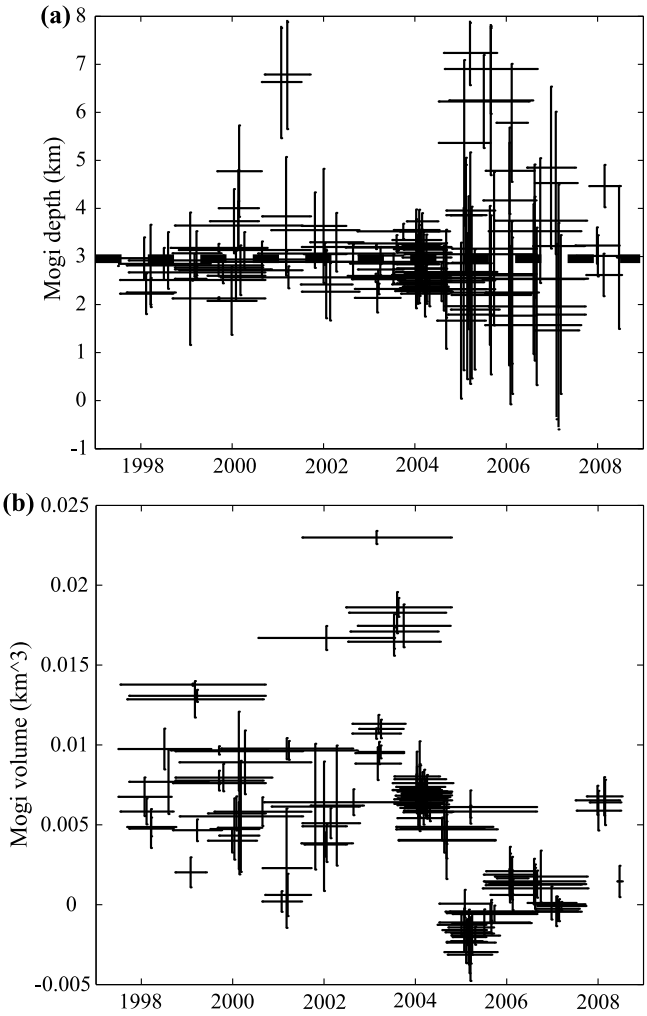

Figure 7. (a) Depth estimates of the best fit Mogi source with associated uncertainties, plotted as a function of time. (b) Volume estimates of the best fit Mogi source with associated uncertainties, plotted as a function of time. Horizontal bars represent time periods spanned by individual interferograms, and vertical bars represent one-sigma error bars (see text for discussion). The weighted average source depth (thick dotted line in Figure 7a) is about 3 km below sea level or 3.5 km beneath the caldera floor.

inflation at Okmok during 1993–1996 and 2004–2007 might indicate critical states of pressurization for the reservoir, in which the surrounding country rock is strong enough to temporarily retard the magma supply from depth. Exsolution of magmatic volatiles during these periods and resulting vesiculation might have triggered the eruptions in 1997 and 2008. Experience at other volcanoes suggests that the more common pattern is a steady or increasing inflation rate as an eruption draws near [*Dvorak and Dzurisin*, 1997]. Therefore, there might be a spectrum between those cases and ones in which the inflation rate slows as a function of time before some other process tips the balance either toward or away from an eruption (e.g., vesiculation or cooling/crystallization, respectively). This possibility recommends caution in the interpretation of a declining inflation rate, especially at basaltic volcanoes.

4.3. Short-Term Deformation Precursor to 1997 Eruption?

[27] Was there significant deformation at Okmok from summer 1996 to February 1997, prior to the start of the eruption on 13 February 1997? Because we do not have any useful InSAR images or other geodetic data for that period, we cannot provide a definite answer to that question. However, based on the deformation trend observed during 2004–2008 prior to the start of the 2008 eruption (i.e., resumption of inflation during 2007–2008 following a period of quiescence during 2004–2007), we suspect that the 1997 eruption likewise was preceded by a period of inflation that lasted several months. Continuous InSAR observations from multiple satellites throughout the next eruption cycle at Okmok will help to test ideas advanced here and refine our understanding of the volcano's magma plumbing system and eruption triggering mechanisms.

5. Conclusion

[28] Multitemporal InSAR images from 3 different radar satellites have been used to map the intereruption deformation of Okmok volcano during 1997–2008. A Mogi point pressure source or a finite sphere with a radius of 1 km provides a good fit to the time series deformation images. Deformation modeling reveals that a shallow magma storage zone centered about ~3.5 km beneath the center of the 10 km diameter caldera floor has been responsible for the observed deformation. The intereruption deformation during 1997–2008 is characterized by an initially rapid inflation followed by oscillatory but generally slowing inflation, suggesting that the magma supply rate decreased with time in response to the

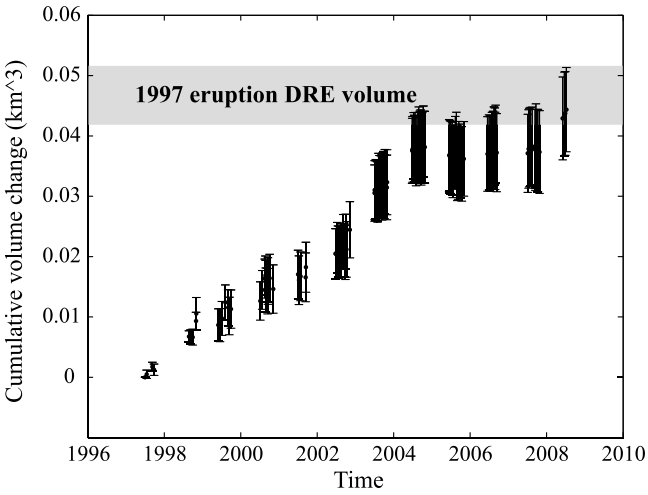

Figure 8. Estimated volume of additional magma stored in the shallow reservoir beneath Okmok as a function of time from 1997 to 10 July 2008. Error bars represent one-sigma uncertainties (see text for discussion). Shaded zone represents the source volume decrease associated with the 1997 eruption, as inferred from a coeruption interferogram [*Lu et al.*, 2005]. The volume of magma withdrawn from the reservoir during the 1997 eruption was largely replenished before the start of the 2008 eruption, perhaps as early as 2004 and more likely by mid-2008.

diminishing pressure difference between the shallow magma storage zone and a deep magma source. The total amount of magma added to the shallow storage zone from the end of the 1997 eruption to a few days before the 2008 eruption was 85–100% of the 1997 eruption volume. Eventually, exsolution of magmatic volatiles and the resulting vesiculation of accumulated magma in the shallow storage zone caused a critical pressure threshold to be exceeded, triggering the 2008 eruption.

[29] In this study, we have again demonstrated that InSAR is a valuable tool for long-term volcano monitoring. Obviously, more frequent SAR image acquisitions would make InSAR more useful for real time monitoring. However, InSAR analysis shows that eruptions at Okmok in 1997 and 2008 were preceded by periods of little or no deformation that lasted 3–4 years and ended less than a year before those eruptions began. This pattern suggests that short-term forecasting based on InSAR-mapped deformation alone might be difficult in some cases. InSAR can effectively track surface deformation from summer to summer, but might not provide a robust indication of an ensuing eruption in the months or weeks beforehand. This is especially true at times when the volcano is covered by snow and InSAR is ineffective. Experience shows that short-term precursors such as localized deformation, seismicity, and changes in volcanic gas emission commonly are observed when a shallow magma reservoir nears rupture or as magma intrudes surrounding rock [e.g., *Benoit and McNutt*, 1996; *Sparks*, 2003]. Such precursors can be detected by in situ sensors and they typically provide days to months of warning (although seismic precursors to the Okmok eruption that began on 12 July 2008 lasted only a few hours). Therefore, effective monitoring and hazards mitigation for a volcano like Okmok requires the integration and analysis of multiple geophysical and geochemical data sets in near-real time.

[30] **Acknowledgments.** Original ERS-2 and Envisat SAR raw data are copyrighted by the European Space Agency (ESA) 1997–2008 and were provided by Alaska Satellite Facility (ASF) and ESA. Original Radarsat-1 raw data are copyrighted by the Canadian Space Agency (CSA) and were provided by ASF. This work is supported by NASA's Earth Surface and Interiors (ESI) program through grant 2005–0021, and by the USGS Volcano Hazards Program and Land Remote Sensing Program. We thank ESA and ASF for their outstanding support in providing SAR data on a timely basis, M. Lisowski and W. McCausland for technical reviews and T. Fournier for discussion of CGPS data and analysis. Constructive comments from Associate Editor R. Lohman and two anonymous reviewers have improved the manuscript.

References

Benoit, J. P., and S. R. McNutt (1996), Global volcanic earthquake swarm database and preliminary analysis of volcanic earthquake swarm duration, *Ann. Geofis.*, *39*, 221–229.

Berardino, P., G. Fornaro, R. Lanari, and E. Sansosti (2002), A new algorithm for surface deformation monitoring based on small baseline differential SAR interferograms, *IEEE Trans. Geosci. Remote Sens.*, *40*, 2375–2383, doi:10.1109/TGRS.2002.803792.

Biggs, J., R. Burgmann, J. Freymueller, Z. Lu, B. Parsons, I. Ryder, G. Schmalzle, and T. Wright (2009), The postseismic response to the 2002 M7.9 Denali Fault Earthquake: Constraints from InSAR 2003–2005, *Geophys. J. Int.*, *176*, 353–367, doi:10.1111/j.1365-246X.2008.03932.x.

Biot, M. A. (1956), Thermoelasticity and irreversible thermodynamics, *J. Appl. Phys.*, *27*(3), 240–253, doi:10.1063/1.1722351.

Briole, P., D. Massonnet, and C. Delacourt (1997), Post-eruptive deformation associated with the 1986–87 and 1989 lava flows of Etna detected by radar interferometry, *Geophys. Res. Lett.*, *24*, 37–40, doi:10.1029/96GL03705.

Dieterich, J. H., and R. W. Decker (1975), Finite element modeling of surface deformation associated with volcanism, *J. Geophys. Res.*, *80*, 4094–4102, doi:10.1029/JB080i029p04094.

Dvorak, J., and D. Dzurisin (1997), Volcano geodesy: The search for magma reservoirs and the formation of eruptive vents, *Rev. Geophys.*, *35*, 343–384, doi:10.1029/97RG00070.

Dvorak, J., and A. T. Okamura (1987), A hydraulic model to explain variations in summit tilt rate at Kilauea and Mauna Loa volcanoes, *U.S. Geol. Surv. Prof. Pap.*, *1350*, 1281–1296.

Dzurisin, D., M. Lisowski, and C. Wicks (2009), Continuing inflation at Three Sisters volcanic center, central Oregon Cascade Range, USA, from GPS, leveling, and InSAR observations, *Bull. Volcanol.*, *71*, 1091–1110, doi:10.1007/s00445-009-0296-4.

Fialko, Y., and M. Simons (2000), Deformation and seismicity in the Coso geothermal area, Inyo conty, California: Observations and modeling using satellite radar interferometry, *J. Geophys. Res.*, *105*, 21,781–21,793, doi:10.1029/2000JB900169.

Fournier, T. (2008), Analysis and interpretation of volcano deformation in Alaska: Studies from Okmok and Mt Veniaminof volcanoes, Ph.D. thesis, Univ of Alaska Fairbanks, Fairbanks, Alsaka.

Fournier, T., J. Freymueller, and P. Cervelli (2009), Tracking magma volume recovery at Okmok volcano using GPS and an unscented Kalman filter, *J. Geophys. Res.*, *114*, B02405, doi:10.1029/2008JB005837.

Freymueller, J., T. Fournier, and A. Kaufman (2008), Deformation of Okmok volcano associated with its 2008 eruption, *Eos Trans. AGU*, *89*(53), Fall Meet. Suppl., Abstract A53B-0260.

Gordon, R. G., S. Stein, C. DeMets, and D. Argus (1987), Statistical tests for closure of plate motion circuits, *Geophys. Res. Lett.*, *14*, 587–590, doi:10.1029/GL014i006p00587.

Grey, D. (2003), Post-caldera eruptions at Okmok volcano, Umnak Island, Alaska, with emphasis on recent eruptions from Cone A., M.S. thesis, Univ. of Alaska Fairbanks, Fairbanks, Alaska.

Jaeger, J. C. (1969), *Elasticity, Fracture and Fluid Flow*, 268 pp., Methuen, London.

Johnson, D. J., F. Sigmundsson, and P. T. Delaney (2000), Comment on "Volume of magma accumulation or withdrawal estimated from surface uplift or subsidence, with application to the 1960 collapse of Kilauea volcano" by P. T. Delay and D. F. McTigue, *Bull. Volcanol.*, *61*, 491–493, doi:10.1007/s004450050006.

Jonsson, S. (2002), Modeling volcano earthquake deformation from satellite radar interferometric observations, Ph.D. thesis, Stanford Univ., Palo Alto, Calif.

Larsen, J., C. Neal, P. Webley, J. Freymueller, M. Haney, S. McNutt, D. Schneider, S. Prejean, J. Schaefer, and R. Wessels (2009), Eruption of Alaska volcano breaks historic pattern, *Eos Trans. AGU*, *90*(20), 173–175, doi:10.1029/2009EO200001.

Lohman, R., and M. Simons (2005), Some thoughts on the use of InSAR data to constrain models of surface deformation: Noise structure and data downsampling, *Geochem. Geophys. Geosystems.*, *6*, Q01007, doi:10.1092/2004GC000841.

Lu, Z., and D. Dzurisin (2010), Ground surface deformation patterns, magma supply, and magma storage at Okmok volcano, Alaska, inferred from InSAR analysis: 2. Coeruptive deflation, July–August 2008, *J. Geophys. Res.*, *115*, B00B03, doi:10.1029/2009JB006970.

Lu, Z., D. Mann, and J. Freymueller (1998), Satellite radar interferometry measures deformation at Okmok Volcano, *Eos Trans. AGU*, *79*(39), 461–468, doi:10.1029/98EO00348.

Lu, Z., D. Mann, J. Freymueller, and D. Meyer (2000), Synthetic aperture radar interferometry of Okmok volcano, Alaska: Radar observations, *J. Geophys. Res.*, *105*, 10,791–10,806, doi:10.1029/2000JB900034.

Lu, Z., T. Masterlark, D. Dzurisin, R. Rykhus, and C. Wicks (2003a), Magma supply dynamics at Westdahl volcano, Alaska, modeled from satellite radar interferometry, *J. Geophys. Res.*, *108*(B7), 2354, doi:10.1029/2002JB002311.

Lu, Z., E. Fielding, M. Patrick, and C. Trautwein (2003b), Estimating lava volume by precision combination of multiple baseline spaceborne and airborne interferometric synthetic aperture radar: The 1997 eruption of Okmok volcano, Alaska, *IEEE Trans. Geosci. Remote Sens.*, *41*, 1428–1436, doi:10.1109/TGRS.2003.811553.

Lu, Z., T. Masterlark, and D. Dzurisin (2005), Interferometric synthetic aperture radar study of Okmok volcano, Alaska, 1992–2003: Magma supply dynamics and post-emplacement lava flow deformation, *J. Geophys. Res.*, *110*, B02403, doi:10.1029/2004JB003148.

Mann, D., J. Freymueller, and Z. Lu (2002), Deformation associated with the 1997 eruption of Okmok volcano, Alaska, *J. Geophys. Res.*, *107*(B4), 2072, doi:10.1029/2001JB000163.

Masterlark, T. (2007), Magma intrusion and deformation predictions: Sensitivities to the Mogi assumptions, *J. Geophys. Res.*, *112*, B06419, doi:10.1029/2006JB004860.

Miller, T. P., R. G. McGimsey, D. H. Richter, J. R. Riehle, C. J. Nye, M. E. Yount, and J. A. Dumoulin (1998), Catalog of the historically active volcanoes of Alaska, *U.S. Geol. Surv. Open File Rep.*, *98–582*, 1–104.

Miyagi, Y., J. Freymueller, F. Kimata, T. Sato, and D. Mann (2004), Surface deformation caused by shallow magmatic activity at Okmok volcano, Alaska, detected by GPS campaigns 2000–2002, *Earth Planets Space*, *56*, e29–e32.

Mogi, K. (1958), Relations between the eruptions of various volcanoes and the deformations of the ground surface around them, *Bull. Earthquake Res. Inst. Univ. Tokyo*, *36*, 99–134.

Patrick, M. R., J. Dehn, K. R. Papp, Z. Lu, L. Moxey, K. G. Dean, and R. Guritz (2003), The 1997 eruption of Okmok Volcano, Alaska: A synthesis of remotely sensed imagery, *J. Volcanol. Geotherm. Res.*, *127*, 87–105, doi:10.1016/S0377-0273(03)00180-X.

Press, W., S. Teukolsky, W. Vetterling, and B. Flannery (1992), *Numerical Recipes in C: The Art of Scientific Computing*, 994 pp., Cambridge Univ. Press, Cambridge, U. K.

Rivalta, E., and P. Segall (2008), Magma compressibility and the missing source for some dike intrusions, *Geophys. Res. Lett.*, *35*, L04306, doi:10.1029/2007GL032521.

Sparks, S. (2003), Forecasting volcanic eruptions, *Earth Planet. Sci. Lett.*, *210*, 1–15.

Stevens, N. F., G. Wadge, C. A. Williams, J. G. Morley, J. P. Muller, J. B. Murray, and M. Upton (2001), Surface movements of emplaced lava flows measured by synthetic aperture radar interferometry, *J. Geophys. Res.*, *106*, 11,293–11,313, doi:10.1029/2000JB900425.

Wang, H. F. (2000), *Theory of Linear Poroelasticity: With Applications to Geomechanics*, 287 pp., Princeton Univ. Press, Princeton, N. J.

Williams, C. A., and G. Wadge (1998), The effects of topography on magma reservoir deformation models: Application to Mt. Etna and radar interferometry, *Geophys. Res. Lett.*, *25*, 1549–1552, doi:10.1029/98GL01136.

Wright, T., Z. Lu, and C. Wicks (2003), Source model for the Mw 6.7, 23 October 2002, Nenana Mountain Earthquake (Alaska) from InSAR, *Geophys. Res. Lett.*, *30*(18), 1974, doi:10.1029/2003GL018014.

Yang, X. M., P. Davis, and J. H. Dieterich (1988), Deformation from inflation of a dipping finite prolate spheroid in an elastic half-space as a model for volcanic stressing, *J. Geophys. Res.*, *93*, 4249–4257, doi:10.1029/JB093iB05p04249.

J. Biggs, Rosenstiel School of Marine and Atmospheric Sciences, University of Miami, 4600 Rickenbacker Cswy, Miami, FL 33149, USA.

D. Dzurisin and Z. Lu, Cascades Volcano Observatory, U.S. Geological Survey, 1300 SE Cardinal Ct., Building 10, Suite 100, Vancouver, WA 98683-9589, USA. (lu@usgs.gov)

S. McNutt, Alaska Volcano Observatory, University of Alaska Fairbanks, 903 Koyukuk Dr., P.O. Box 757320, Fairbanks, AK 99775-7320, USA.

C. Wicks Jr., U.S. Geological Survey, MS 977, 345 Middlefield Rd., Menlo Park, CA 94025, USA.